

On the calculation of an attenuation coefficient for transects of ice-covered ocean

Luke G. Bennetts and Vernon A. Squire

*Department of Mathematics and Statistics, University of Otago, P. O. Box 56, Dunedin
9054, New Zealand.*

Exponential attenuation of ocean surface waves in ice-covered regions of the polar seas is modelled in a two-dimensional, linear setting, assuming the sea ice behaves as a thin-elastic plate. Attenuation is produced by natural features in the ice cover, with three types considered: floes, cracks and pressure ridges. An inelastic damping parameterization is also incorporated. Efficient methods for obtaining an attenuation coefficient for each class of feature, involving an investigation of wave interaction theory and averaging methods, are sought. It is found that (i) the attenuation produced by long floes can be obtained from the scattering properties of a single ice edge; and (ii) wave interaction theory requires evanescent and damped-propagating motions to be included when scattering sources are relatively nearby. Implications for the integration of this model into an oceanic general circulation model are also discussed.

Key words: Surface gravity waves, sea ice, attenuation coefficient.

1. Introduction

A significant corpus of research now exists describing how sea ice affects and is affected by ocean surface waves, noting that the major part of this work consists of mathematical modelling. Considerable effort has been put into understanding how the intensity of waves reduces with distance into the ice covered ocean, and, to a lesser extent, how the sea ice itself is altered by the waves. While not the main focus of this paper, the latter's consequences for sea ice are actually highly topical because in the Arctic, particularly, the sea ice is adapting to global warming by becoming thinner, less concentrated and physically weaker (Wadhams & Davis, 2000; Serreze et al., 2007; Kwok & Rothrock, 2009) and it is probable that ocean waves will accelerate this enfeebling transformation.

A period of rapid advancement in the understanding of the effects of sea ice on ocean swell occurred in the 1970s–80s through programmes run by the Scott Polar Research Institute, UK. Experimental recordings due to Wadhams (1973, 1986), and associated papers, and Wadhams et al. (1986, 1988) first demonstrated an exponential decay of wave intensity with distance into ice-covered regions, with a rate depending predominantly on wave period and ice thickness. A relationship with wave scattering was established, and theoretical models were developed that accorded with the experimental advances. Although insubstantial field data have appeared since this pioneering era, theoretical advances have continued unabated (Squire, 2007), building on the original model of Wadhams (1973). With certain exceptions, e.g. Bennetts et al. (2010), work is still restricted to two-dimensions but has reached a level of sophistication at which a numerical description of wave evolution through an ice pack that resembles natural

sea ice in situ is possible (Kohout & Meylan, 2008; Vaughan et al., 2009; Squire et al., 2009). Perhaps most significantly, it is now understood that multiple scattering must be considered in conjunction with wave coherence effects and wave localization theory for the model to exhibit the observed exponential decay properly (Berry & Klein, 1997). One of the purposes of the present investigation is to clarify this relationship.

An overriding goal driving the theoretical advances has been to properly embed interactions between ocean waves and sea ice into ice/ocean models and general ocean circulation models (OGCMs) — an attribute of sea ice dynamics that is currently conspicuous by its absence. Mathematical models are primarily intended to explain how ocean wave trains evolve spatially as they proceed through fields of sea ice. However, in an OGCM these results have a direct bearing on sea ice morphology too because the capacity to damage floes will depend on the local wave energy. This interdependence is the basis for a recently proposed one-(horizontal)-dimensional ice/ocean model (Dumont et al., 2011), which is currently being extended to an operational two-dimensional model, i.e. the ocean surface, and is seen as a precursor to full assimilation into an OGCM. The work presented in this paper is intended to provide the wave evolution kernel for such models, and seeks methods and approximations to alleviate some of their computational load, which is particularly acute in the two-dimensional setting.

Natural sea ice floating in the ocean can take several forms that affect the passage of ocean waves and swells variously, most notably by reducing their amplitude. Near the ice edge, i.e. the boundary between the open ocean and the start of the ice cover, the ice is typically fragmented, as aggressive seas infiltrate the ice canopy causing local floes to bend, fatigue and fracture when they are too large. In extreme seas the pummelling can create an outer band of ice slurry a few kilometres across, where it is difficult to distinguish individual floes, or an expanse of heavily-deformed rafted sea ice. A little further into the ice pack, the seas will have lost some of their ferocity but they still control the floe size distribution by breaking up substantial floes (Toyota et al., 2011). These portions of the ice cover are known collectively as the marginal ice zone, usually denoted MIZ. The MIZ is an interfacial region that resides at the fringe of the open and frozen oceans, neither fully open nor fully frozen over — a *mélange* of ice cakes and floes, habitually pervaded by slurries of frazil ice and brash. Because the MIZ is the part of the ice cover closest to open sea, it is a very dynamic region that is affected majorly by incoming ocean waves and swells and changes of wind and current. Concentration is generally variable, both spatially and temporally, and the nature of the ice floes making up the zone is also normally quite heterogeneous as the waves break up floes differentially.

Beyond the MIZ, after the advancing wave trains have been attenuated sufficiently that they no longer have the capability to fracture the ice floes, the sea ice becomes quasi-continuous. On the whole, floes there are vast with the underlying heterogeneity expressed through features such as cracks, open and refrozen leads, pressure ridge sails and keels, and variations in the mechanical and physical properties such as thickness, attributable to growth history and lateral rafting events caused by currents and winds. In the current work these regions will be referred to as the quasi-continuous ice cover and abbreviated to QCIC.

Free surface ocean waves propagating into and travelling through pack ice can therefore expect to encounter several different kinds of irregularity during their passage, particularly depending on physical location. Notwithstanding this, from a modelling perspective their progression will be determined by: (i) scattering from a distribution

of sizes of discrete ice floes, present at some specified concentration, in the MIZ; and (ii) reflections from natural imperfections in the quasi-continuous ice interior. In addition, energy will be lost from the advancing wave trains because of ‘turbulence’ in the water, the natural inelasticity of the sea ice and, when the seas are rough, collisions between adjacent ice floes that are provoked by relentless wave action. Each of these mechanisms causes some diminution of the wave amplitude in a manner that is known to favour the passage of long period waves over short periods, so, as explained in the reviews by Squire et al. (1995) and Squire (2007), the integrated effect of coming upon many heterogeneities over large distances is a gradual evolution of the wave spectrum towards longer period energy and the elimination of short period waves.

2. Preliminaries

A two-dimensional fluid domain is considered and will be defined using the Cartesian coordinates x , in the horizontal direction, and z , in the vertical direction. The vertical coordinate is orientated upwards and has its origin set to coincide with the equilibrium surface of the fluid (in the absence of ice cover). The fluid domain extends to infinity in both horizontal directions, and its bed is flat and is located at $z = -h$. For the prototype numerical investigations conducted in the present work h is set as 250 m, as this value is sufficiently deep that its influence is negligible.

The fluid is assumed to be inviscid, incompressible, homogeneous, and in irrotational motion. As the intention is to investigate wave attenuation as a function of wave period τ , a periodic time-dependence of a prescribed angular frequency $\omega = 2\pi/\tau$, is assumed. The fluid’s velocity field may therefore be defined as the gradient of a scalar velocity potential $\text{Re} \{(g/i\omega)\phi(x, z)e^{-i\omega t}\}$, where $g \approx 9.81 \text{ m s}^{-2}$ is acceleration due to gravity, and ϕ is a (reduced) velocity potential that must be calculated.

For all points in the fluid domain the velocity potential satisfies Laplace’s equation

$$\partial_x^2 \phi + \partial_z^2 \phi = 0, \quad (2.1)$$

where $(\partial_x, \partial_z) \equiv (\partial/\partial x, \partial/\partial z)$. The impermeable-bed and free-surface conditions,

$$\partial_z \phi = 0 \quad (z = -h), \quad \text{and} \quad \partial_z \phi = \sigma \phi \quad (z = 0), \quad (2.2)$$

respectively, where $\sigma = \omega^2/g$ is a frequency parameter, are also applied, with the latter condition holding at the points where the ice cover is absent.

A covering of sea ice extends over a proportion (possibly all) of the fluid’s surface. Three different features in the ice cover will be considered and are described in the forthcoming subsections. Fluid motion causes the ice to flex and the resulting position of the lower surface of the ice is defined as $z = -d(x) + \text{Re} \{w(x)e^{-i\omega t}\}$. Here $d = \rho_i D/\rho_w$ denotes the draught of the ice, where $D = D(x)$ is the ice thickness, and ρ_i and ρ_w denote the densities of the ice and fluid, respectively. The quantity w is a displacement function that will be obtained as part of the solution process.

Due to the large lateral dimensions of sea ice in relation to its thickness, it is customary to model its motion using thin-plate theory. Combining this with the linearized Bernoulli equation and the assumption of no cavitation between the fluid and ice, leads to the coupling between the velocity potential and the displacement function

$$(1 - \sigma d)w + Fw'''' = \phi \quad (z = -d), \quad (2.3a)$$

where a prime denotes differentiation with respect to x , and which is applied at the linearized fluid-ice interface. (This form of the equation assumes that the properties of the ice are uniform in a neighbourhood of the point x .) A second coupling is derived from the linearization of the kinematic condition, to give

$$\partial_z \phi = \sigma w \quad (z = -d). \quad (2.3b)$$

The development of equations (2.3a–b) can be traced to, e.g., Wadhams (1973, 1986).

In equation (2.3a) the quantity $F = F(x)$ is a scaled version of the flexural rigidity of the ice. It is defined by $F = YD^3/\{12(1 - \nu)\rho_w g\}$, in which $\nu = 0.3$ is the effective Poisson's ratio for sea ice, and $Y = 6 \text{ G Pa}$ is the effective Young's modulus for sea ice. The latter is a value that is regularly used in idealised wave-ice models, although it does not represent all ice types. It varies with brine volume, and is typically less for multi-year ice than first-year ice (Timco & Weeks, 2010). The following analysis will remain applicable for any chosen value of Young's modulus. Some specific examples of the effects of changing its value will be given for the case of ridges. However, a thorough sensitivity analysis of wave-ice interactions to variations in the Young's modulus is not commensurate with the objectives of the current investigation. It is noted that when the flexural motion of the ice dominates its response to fluid motion, i.e. when the value of the Young's modulus is important, its variations are equivalent to variations in the cube of the ice thickness.

The fluid-ice coupling defined in equations (2.3a–b) is intended for use in the scattering regime, in which wavelengths are comparable to floe diameters. More sophisticated models are required to incorporate additional dissipative mechanisms. Work in this area is ongoing, and, in particular, a viscoelastic model to parameterize the compounded effects of different sea ice types has been proposed recently (see Wang & Shen, 2010).

Equations (2.1)–(2.3) are solved for ϕ and w , along with appropriate radiation conditions, which ensure that the solution in the far field involves only the incident wave field and waves scattered by any features in the ice cover. Forcing is produced by an incident wave of unit amplitude, propagating from $x \rightarrow -\infty$.

It will be of use in the subsequent analysis to note that in intervals of uniform geometry, i.e. a constant ice thickness (and draught) or no ice cover, an expression may be found for the velocity potential as the superposition of waves. From this, a similar expression can be found for the displacement function through equation (2.3b).

When ice is not present, this takes the form

$$\phi(x, z) \approx \sum_{n=0}^N \{a_n e^{ik_n x} + b_n e^{-ik_n x}\} \xi_n(z), \quad \xi_n(z) = \cosh\{k_n(z + h)\}, \quad (2.4)$$

where a_n and b_n are complex-valued constants that depend on the surrounding geometry. The quantities k_n are wavenumbers that are calculated as the roots k of

$$k \tanh(kh) = \sigma,$$

which is the free-surface dispersion relation. The primary wavenumber, k_0 , is real and positive. It supports propagating waves: incident, reflected and transmitted. The corresponding coefficients a_0 and b_0 carry an amplitude and a phase. All remaining wavenumbers, k_n ($n = 1, 2, \dots$), lie on the positive imaginary axis and are ordered in increasing magnitude. They support evanescent waves, generated during the scattering process, which are local surface deflections that decay exponentially with distance away

from the scattering source. The rate of decay is determined by the magnitude of the wavenumber, so that the least rapidly decaying waves appear first in the summation. For the purposes of a numerical solution, the series in the above representation is truncated at some non-negative integer value N , which is chosen to be sufficiently large that a desired accuracy is obtained.

In intervals of constant ice thickness, the velocity potential has the form

$$\phi(x, z) \approx \sum_{n=-2}^N \{\alpha_n e^{i\kappa_n x} + \beta_n e^{-i\kappa_n x}\} \eta_n(z), \quad \eta_n(z) = \cosh\{\kappa_n(z+h)\}. \quad (2.5)$$

In this case the wavenumbers are denoted κ_n , and are the roots κ of

$$(1 - \sigma d + F\kappa^4)\kappa \tanh\{\kappa(h-d)\} = \sigma,$$

which is the ice-covered dispersion relation (e.g. Squire, 2007). As in the free surface case, the primary wavenumber, κ_0 , is real and positive and the wavenumbers κ_n ($n = 1, 2, \dots$) lie on the positive imaginary axis. Therefore, propagating and evanescent modes are both supported. For moderate to large wave periods the propagating waves are typically longer than their free-surface counterparts and increase in length with rigidity, i.e. thickness. However, for small periods this is not necessarily the case.

The coupling of the fluid and ice generates an additional type of motion not present in open water. These motions are described as damped-propagating waves, as they possess a phase, an amplitude and an exponential decay rate. Their wavenumbers, κ_{-n} ($n = 1, 2$), exist in the upper-half complex plane, and are mirror images of one another in the imaginary axis. In terms of the governing equations, the damped-propagating waves are a product of the high-order boundary condition (2.3a). Their presence removes the usual orthogonality of the wave motions in the vertical plane.

For the governing equations given above, no wave energy will be lost from the overall system. However, the methods presented in this work are intended to accommodate more general cases in which forms of inelastic wave damping are incorporated. Damping properties enter the problem through an imaginary component in the ice-covered dispersion relation and may act as a parameterization of viscous or hysteresis losses. The effect of an imaginary component in the dispersion relation is to perturb the wavenumbers, so that they no longer lie on the real/imaginary axes. In particular the primary wavenumber takes on a small imaginary component and therefore becomes $\kappa_0 + i\epsilon$.

(a) Floes

A floe is considered to be an interval of ice cover of finite length, separated from any surrounding intervals of ice cover by open water. For the present study it is assumed that each floe has a constant thickness and thus scattering is produced by the ice edges alone.

At an edge of a floe, $x = x_0$ say, the free motion of the plate results in the dynamic conditions $w'' = w''' = 0$, which represent the vanishing of the floe's bending moment and shearing stress, respectively. Furthermore, no lateral motion of the floes is permitted, and therefore the horizontal fluid velocity is set to zero on the submerged portion of the ice edge, that is $\partial_x \phi = 0$ ($-d < z < 0$), where x tends to x_0 from the appropriate limit.

(b) Cracks

A crack is formed when the length of an open water interval between two ice edges tends to zero. The above dynamic conditions remain, but the kinematic condition is not required. Simple modifications to the crack model are possible. For instance, a small length of open water may be allowed to remain between the ice edges, which would model a lead.

(c) Pressure Ridges

A pressure ridge is a finite interval, in an otherwise uniform ice cover, in which the thickness varies. It is possible to calculate the scattering produced by a smoothly varying thickness variation of this kind (see Bennetts et al., 2007). However, here the thickness profile of the pressure ridges considered will instead be discretized and the mesh refined until convergence of the scattering properties is achieved to a satisfactory accuracy.

The aim of the present work is to determine the attenuation produced by each of these three features. To achieve this, a large but finite number, M say, of commensurate features are considered to occupy the ice-covered region of the fluid domain. As in, e.g., Kohout & Meylan (2008), the transmitted energy is calculated as a function of M and an exponential curve fitted to an ensemble average of this data in order to extract the rate of exponential attenuation, which is known as the (non-dimensional) attenuation coefficient, μ say. This has proved to give very similar results to a method in which the attenuation coefficient is calculated from a snapshot of the surface displacement (e.g. Vaughan et al., 2009), but is more stable for large periods.

The investigation is split into, firstly, that of the wave interactions between features and, secondly, the scattering properties of the individual features. It will be seen later that this order gives the most natural flow to the analysis.

3. An approximation for multiple features

The calculation of an attenuation coefficient is computationally demanding, with the result that approximation methods are popular. Wadhams (1973, 1986), for example, proposed such a method for multiple floes where the underlying assumptions are that (i) no evanescent deflections arise at respective ice edges so that only continuity of the surface pressure and the free-edge conditions can be satisfied; (ii) no backscatter occurs, wave phases are ignored, and floes are assumed long enough that the damped-propagating waves do not contribute to wave interactions within and between floes. A correction for double scattering was also given. In fact, however, scattering actually involves an infinite sequence of reflections between any two interfaces and, as explained by Berry & Klein (1997), exponential decay follows as a result of wave coherence, i.e. phase interactions, and positional disorder, i.e. it is a localization effect. This property is visible in the results of Kohout & Meylan (2008), where the full solution for an individual floe is also implemented. The extension to multiple features in a QCIC is new to the current study.

Computational expense is derived from three main sources. The first is in calculating the scattering properties for a large number of individual features. The second is in combining these scattering properties to obtain the scattering properties of the set of

features. Finally, these processes must be repeated a large number of times to form an ensemble. It is important to note that resonance effects due to wave coherence, which are unrepresentative of the physical phenomenon, appear if too much repetition is contained in the geometry. For this reason, a sufficient amount of variation must be included.

The second expense can be alleviated, to some degree, in a two-dimensional setting, by employing an iterative method for calculating the amplitudes between scatterers. Take the case of two adjacent features, a distance s apart. Let the set of amplitudes (including phases) of the rightward and leftward travelling waves for these features be denoted by the vectors $\mathbf{A}_{n\pm}$ and $\mathbf{B}_{n\pm}$, respectively. The subscript indicates whether the amplitudes belong to waves associated with the feature on the left ($n = 1$) or on the right ($n = 2$), and whether the waves are on the left ($-$) or right ($+$) of the feature. The phases of the waves are normalized with respect to the appropriate edge of the relevant feature. For a feature embedded in an ice-covered fluid region, i.e. a crack or a pressure ridge, the amplitude vectors are $\mathbf{A} = [\alpha_0, \dots, \alpha_N, \alpha_{-1}, \alpha_{-2}]^T$ and $\mathbf{B} = [\beta_0, \dots, \beta_N, \beta_{-1}, \beta_{-2}]^T$, whereas, if the feature exists in an otherwise ice-free fluid interval, i.e. the feature is an ice floe, the amplitude vectors are $\mathbf{A} = [a_0, \dots, a_N]^T$ and $\mathbf{B} = [b_0, \dots, b_N]^T$.

The scattering properties of the individual features are encapsulated in their reflection and transmission matrices, $\mathcal{R}_{n\pm}$ and $\mathcal{T}_{n\pm}$ ($n = 1, 2$), respectively, where

$$\mathbf{B}_{n-} = \mathcal{R}_{n-}\mathbf{A}_{n-} + \mathcal{T}_{n+}\mathbf{B}_{n+}, \quad \mathbf{A}_{n+} = \mathcal{T}_{n-}\mathbf{A}_{n-} + \mathcal{R}_{n+}\mathbf{B}_{n+}. \quad (3.1)$$

These matrices relate the amplitudes and phases of the scattered and incident waves, and allow for forcing from decaying waves in addition to travelling waves, which is necessary between features.

The corresponding reflection and transmission matrices for the two features acting together, $\mathcal{R}_{1,2\pm}$ and $\mathcal{T}_{1,2\pm}$ say, can be calculated by combining the reflection and transmission matrices for the individual features, to produce the identities

$$\mathcal{R}_{1,2\pm} = \mathcal{R}_{j_{\pm}\pm} + \mathcal{T}_{j_{\pm}\mp}\Lambda\mathcal{M}_{j_{\mp},j_{\pm}}, \quad \text{and} \quad \mathcal{T}_{1,2\pm} = \mathcal{T}_{j_{\pm}\pm}\Lambda\mathcal{M}_{j_{\pm},j_{\pm}}, \quad (3.2)$$

where $j_- = 1$, $j_+ = 2$, and

$$\begin{pmatrix} \mathcal{M}_{1,1} & \mathcal{M}_{1,2} \\ \mathcal{M}_{2,1} & \mathcal{M}_{2,2} \end{pmatrix} = \begin{pmatrix} \mathcal{I} & -\mathcal{R}_{1+}\Lambda \\ -\mathcal{R}_{2-}\Lambda & \mathcal{I} \end{pmatrix}^{-1} \begin{pmatrix} \mathcal{T}_{1-} & 0 \\ 0 & \mathcal{T}_{2+} \end{pmatrix},$$

in which \mathcal{I} is an identity matrix. The matrix Λ contains the phase changes of the waves between the features and is defined as $\Lambda = [e^{ik_0s}, \dots, e^{ik_Ns}]$ when the fluid surface between the features is ice free and $\Lambda = [e^{i\kappa_0s}, \dots, e^{i\kappa_Ns}, e^{i\kappa_{-1}s}, e^{i\kappa_{-2}s}]$ when it is ice covered. The notation $[\cdot]$ denotes a diagonal matrix.

The above identity is not the most common form of such expressions, but allows for the number of waves considered in the interaction theory to differ, which is required when moving from an open water domain to an ice-covered fluid domain, for instance. The scattering matrices for the entire set of features, $\mathcal{R}_{1,M\pm}$ and $\mathcal{T}_{1,M\pm}$, may thus be calculated by beginning with the leftmost two features and repeatedly applying the above identities with each additional feature until the rightmost feature is reached.

The size of the matrices that must be inverted at each step of this iterative algorithm depends on the number of waves considered in the interaction theory, i.e. the value of N . Computational efficiency therefore relies on selecting the minimum value of N that will maintain accuracy. Keeping the number of waves used in the interaction theory to a small value also allows for analytical insight to be gained.

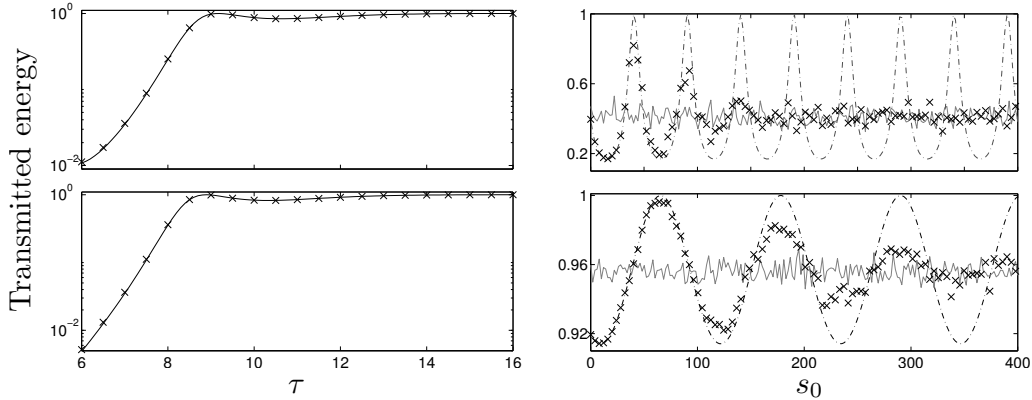


Figure 1. The left-hand panels compare approximations of the energy transmitted by two floes, as a function of wave period. The solid curves denote the WSA and the crosses denote the converged approximations (4 evanescent waves). The top panel is the case in which the floes are separated by 1 m and the bottom panel is a 5 m separation. The right-hand panels compare the transmitted energy produced using different methods for averaging the separation of the two floes, and as a function of a separation parameter. The black-broken curves are the unaveraged results, the crosses are produced by a Gaussian distribution and the grey curves use a uniform distribution over half a wavelength. The top panel shows results for an 8 s wave period and the bottom panel is for a 12 s period.

(a) *The marginal ice zone*

In the left-hand panels of figure 1 the number of waves required in the interaction theory between two floes is investigated. For the cases shown in these two panels, the floes are identical, with thickness 3 m and length 100 m. The transmitted energy is plotted as a function of wave period for the two separations $s=1$ m and 5 m. The solid curves denote results in which interactions involve only the propagating waves, known conventionally as a wide-spacing approximation (WSA), so called because in this limit the evanescent waves generated at one scattering source do not interact with other scatterers. Results are also shown for interactions involving 4 evanescent waves in addition to the propagating waves (crosses, $N=4$). This number is sufficient that the results will only change negligibly if additional evanescent waves are added.

The similarity between the corresponding WSA and the approximation that includes evanescent waves is compelling. Only a minute difference is visible between the two approximations for the 1 m separation and only for the smaller wave periods. Moreover, it has been found (in results not displayed) that accuracy is maintained by the WSA for a full MIZ. From this point on the WSA will therefore be used for interactions between floes.

In the right-hand panels of figure 1 the transmitted energy produced by the same two floes is considered as a function of the floe separation parameter s_0 . Results are shown for two wave periods, $\tau=8$ s and 12 s. The black-broken curves show the case in which the floe separation is unaveraged, so that s_0 is the separation between the floes. Its simple periodic structure is due to the fact that no wave energy is lost as waves travel through intervals of uniform geometry. The floe separation merely alters the phase of the wave interactions.

The structured behaviour given by this approach is not representative of the physical situation being modelled. In comparison, the crosses in figure 1 show cases in which the floe separation is given a Gaussian distribution with mean s_0 . Results are calculated as the average of 50 randomly generated simulations. The standard deviation of the distribution is set to be one-tenth of the mean floe separation.

It is apparent that, for small separations, the results given by this Gaussian distribution follow those of the unaveraged data. This is simply because the standard deviation of the distribution is small at this stage. As the floe separation, and hence the distribution of separations, increases, the results from the Gaussian distribution deviate from those of the unaveraged case.

At an average separation of approximately 1.5λ , where λ , the incident wavelength, is equal to approximately 100 m for an 8 s wave period and 225 m for a 12 s wave period, the results calculated using a Gaussian distribution settle to a relatively constant value. This value coincides with the grey curves, which are results calculated from an ensemble average in which the floe-separation distribution is uniform over half of an incident wavelength, $\lambda/2$. Such a result is to be expected and would be true for distributions other than a Gaussian, when the root mean squared separation becomes sufficient large, specifically $> \lambda/2$. Insensitivity to floe separation is thus a natural consequence of seeking a transmitted energy free of a resonant structure, using the current model.

Giving the separation a uniform distribution over half a wavelength is nothing more than an average over all possible phases of the propagating waves between the floes — a concept that is consistent with the basis of random linear wave theory (Krogstad, 2005). The above analysis therefore clarifies the relationship between this concept and the distribution of floes (or, more generally, widely-spaced scatterers) used in the current model.

The above findings suggest the use of an averaging technique that was conceived by Berry & Klein (1997) to describe the scattering of optical waves. It allows for the transmission produced by any number of scatterers, averaged over all possible phases, to be found from the properties of the individual scatterers, with no averaging required. In order to implement the technique, it is necessary to use logarithmic averaging.

Consider, therefore, two features and define their log-averaged transmission to be

$$\langle \langle \log |T_{1,2-}|^2 \rangle \rangle = \left\langle \frac{2}{\lambda} \int_{s_0}^{s_1} \log |T_{1,2-}|^2 ds \right\rangle, \quad (3.3)$$

where $\langle \cdot \rangle$ denotes averaging over the properties of the individual feature, which for a floe are its length and thickness. Using the second element of (3.2), along with the WSA, in (3.3) and manipulating the resulting expression in the manner of Berry & Klein (1997), it is found that

$$\langle \langle \log |T_{1,2-}|^2 \rangle \rangle = \langle \log |T_{1-}|^2 \rangle + \langle \log |T_{2-}|^2 \rangle. \quad (3.4)$$

Repeating this procedure systematically gives the log-averaged transmitted energy for the entire transect of floes to be

$$e^{\langle \log |T_{1,M-}|^2 \rangle} = e^{M \langle \log |T_{0-}|^2 \rangle},$$

where the notation $\langle \log |T_{0-}|^2 \rangle \equiv \langle \log |T_{1-}|^2 \rangle = \dots = \langle \log |T_{M-}|^2 \rangle$ has been used for the energy transmitted by a single feature. The corresponding attenuation coefficient is

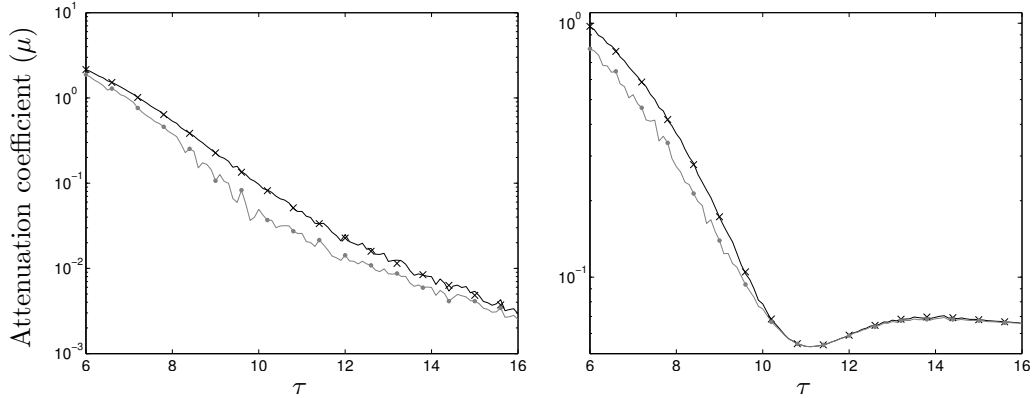


Figure 2. The attenuation coefficient as a function of wave period. The left-hand panel is for a MIZ with identical floes of length 100 m and thickness 3 m. The right-hand panel is for a QCIC of 3 m thickness containing cracks, and the primary wavenumber is given an imaginary component of magnitude 10^{-4} . In both cases the WSA is used to calculate the wave interactions between features and the distribution of their separations is uniform over half a wavelength. The solid curves show results calculated using ensembles with arithmetic (light grey, dotted) and geometric (i.e. logarithmic, black) averaging. The crosses are semi-analytic expressions.

therefore given by the simple expression

$$\mu = -\langle \log |T_{0-}|^2 \rangle. \quad (3.5)$$

A similar expression was used by Williams & Squire (2010) for estimation of the thickness of an ice sheet containing multiple cracks.

The left-hand panel of figure 2 compares the attenuation coefficients produced by standard averaging and logarithmic averaging, i.e. the arithmetic and geometric averages. As in the previous cases considered in this section, the floes have length 100 m and thickness 3 m. Although there is a clear gap between the values given by the two averaging methods, particularly for the mid-range periods, the attenuation coefficients are similar both quantitatively and qualitatively. Most importantly, for the results shown here and in other tests that are not presented, the attenuation coefficients are identical to the first significant figure.

The semi-analytic expression (3.5) is overlaid on the figure. It is almost identical to the values calculated from the ensemble average, with the noise from the latter being the only visible difference. Note that, in the situation used to produce these results there is no averaging of the individual features, so that the brackets $\langle \cdot \rangle$ in equation (3.5) are irrelevant.

(b) Quasi-continuous ice coverings

Wave interactions between features in QCICs, here cracks and pressure ridges, must be considered separately to those that occur between floes. This is due to the presence of damped-propagating waves in intervals of ice-covered fluid, and is evident from comparison of expressions (2.4) and (2.5), recalling that the wavenumbers for damped-propagating waves are denoted κ_{-n} ($n = 1, 2$).

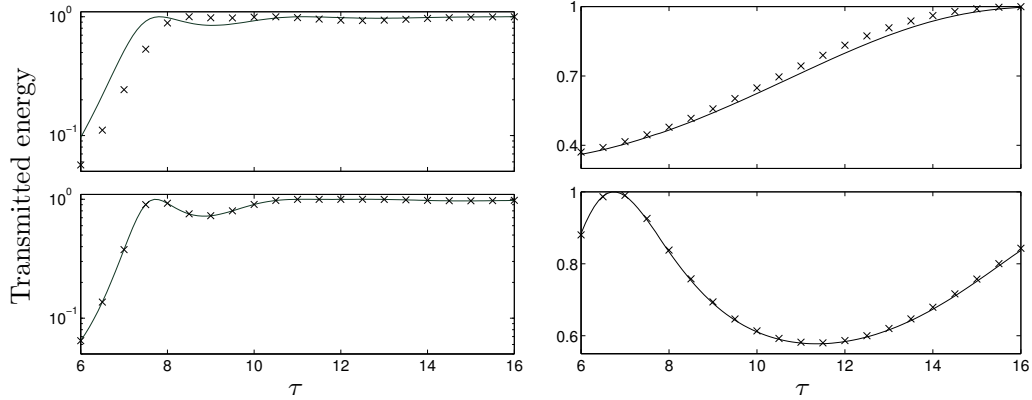


Figure 3. Comparisons of approximations of the energy transmitted by two features in a QCIC, as a function of wave period. The left-hand panels are the results for two cracks in a 3 m-thick ice cover, and the right-hand panels are for two identical ridges, of width 50 m and height 20 m, in otherwise 3 m-thick ice cover. The separation of the cracks is 100 m (top panel) and 200 m (bottom). The separation of the ridges is 50 m (top panel) and 100 m (bottom). The solid curves denote the WSA and the crosses denote approximations that use the damped-propagating waves in addition to the propagating waves in the interaction theory.

Numerical investigations indicate that the damped-propagating waves can have a significant effect on interactions between features. Examples of this are given in figure 3, which shows the energy transmitted by two features in an ice covering of 3 m thickness, as a function of wave period. The corresponding results compare values calculated using the WSA (solid curves) and an approximation in which the damped-propagating waves are included in addition to the propagating waves (crosses).

The left-hand panels show results for two cracks. For a 100 m separation (top panel) there are clear qualitative and quantitative differences between the results given by the WSA and an approximation that includes the damped-propagating waves. As would be expected, the difference is greatest for small wave periods. The performance of the WSA here is in stark contrast to that seen previously for floes in the left-hand panels of figure 1, for which only a negligible change in the transmitted energy was produced by the addition of evanescent waves, and at only a 1 m separation. However, for a 200 m separation of the cracks (bottom panel), the amplitudes of damped-propagating waves have decayed sufficiently that they have no influence on the wave interactions.

The right-hand panels are for two identical rectangular pressure ridges, with width 50 m and height 20 m. Although the inclusion of the damped-propagating waves affects the results for a 50 m separation (top panel), it is far less pronounced than the case of cracks separated by 100 m. At a 100 m separation (bottom panel) there is no visible difference between the WSA and the approximation that includes the damped-propagating waves.

It is interesting to note that the influence of the damped-propagating waves on the wave interactions between features here is greater than that of the evanescent waves, not because they decay less rapidly but because they are generated more strongly by the features. As the examples given in figure 3 demonstrate, this is particularly true for cracks. Moreover, the influence of the damped-propagating waves is dependent on ice thickness, so that, generally, the WSA is valid for shorter separations when ice is thinner between features.

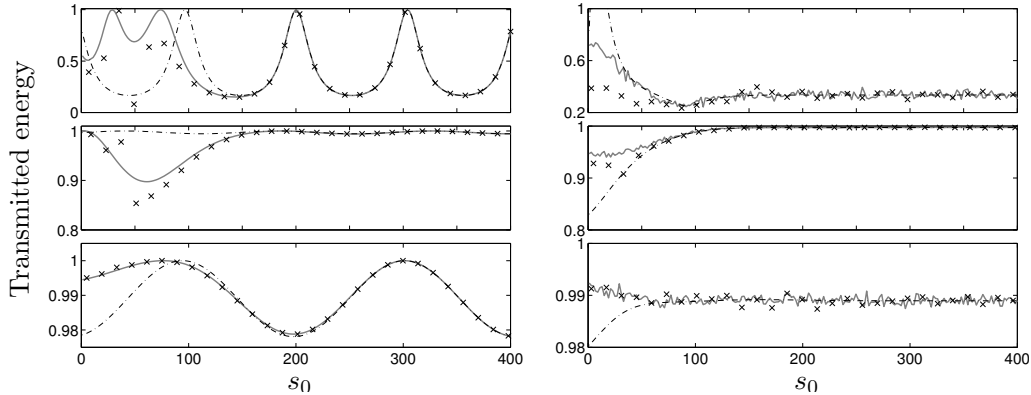


Figure 4. The left-hand panels compare approximations to the energy transmitted by 2 cracks in 3 m-thick QCIC, as a function of their separation. The black-broken curves denote the WSA, the crosses are approximations that include the damped-propagating waves, and the grey curves are converged approximations. The three panels show results for wave periods 8 s (top), 12 s (middle), and 16 s (bottom). The right-hand panels are corresponding results in which the separation obeys a uniform distribution over half a wavelength. Results are calculated using ensemble averages, in which the wave interactions involve only the propagating and damped-propagating waves (crosses) or have converged (grey curves). The black-broken curves are the second-order semi-analytic approximations in terms of the decaying component of the damped-propagating waves.

The left-hand panels of figure 4 compare approximations of the transmitted energy produced by two cracks, as a function of their separation, for the three periods $\tau = 8$ s, 12 s and 16 s. As predicted by the previous results, the approximation that includes the damped-propagating waves (crosses) is distinct from the WSA (black-broken curves) for separations smaller than approximately $s_0 = 150$ to 200 m. The point at which the deviation between the two curves occurs appears to increase as the period gets larger, although the difference between the two curves is generally smaller for larger periods.

For separations less than 50 m an unexpected and spurious resonance is present in the transmitted energy produced by the interactions involving damped-propagating and propagating waves. This is particularly apparent for 8 s and 12 s periods but is also evident at 16 s period. However, by including a small number of evanescent waves the resonances are eliminated. Converged results are shown by the grey curves. At 8 s period 8 evanescent waves are required and for 12 s and 16 s periods 4 evanescent waves are required. A resonance is not produced when the scattering properties for the individual feature are approximated using a dimension (defined in § 4) that is consistent with the interaction theory (examples not shown).

Away from the resonances the results given by the approximations, with and without the evanescent waves, are very similar, although a difference is still visible for 8 s period at small separations. It is therefore evident that the damped-propagating waves are the dominant additional contributors to wave interactions at small separations. However, despite this, the examples given in the left-hand panels of figure 4 clearly demonstrate that it is necessary to include a number of the evanescent waves in the interaction theory for closely spaced features in a QCIC. Without them the transmitted energy can be highly inaccurate around the resonant points.

This is in contrast to the earlier findings for wave interactions in open water, in which the contribution of the evanescent waves was negligible, even for small separations. The reasons behind such a fundamental difference are not currently understood. However, it is assumed that it is related to the non-orthogonality of the natural modes $\{\eta_n\}$ in regions of ice-covered fluid, and the subsequent requirement that each of these modes supports a proportion of the damped-propagating waves.

For the separations at which the damped-propagating and evanescent waves influence the transmitted energy, expression (3.4), which is based on the scalar versions of relations (3.2), is invalid. Instead, the matrix extensions of the relations (3.2), which include the damped-propagating waves and a sufficient number of the evanescent waves, must be adopted. The resulting analysis is far less tractable than the scalar counterpart. However, if the evanescent waves are neglected, it can be shown (after labourious algebra) that the log-average of the energy transmitted by two features may be written

$$\langle \langle \log |T_{1,2-}|^2 \rangle \rangle = \langle \log |T_{1-} T_{2-}|^2 \rangle + \langle c_1 \rangle K + \langle c_2 \rangle K^2 + \dots, \quad (3.6)$$

where $K \equiv e^{-\text{Im}(\kappa_{-1})\hat{s}} = e^{-\text{Im}(\kappa_{-2})\hat{s}}$, in which $\hat{s} = s_0 + \lambda/4$ is the mean separation. The coefficients c_i ($i = 1, 2, \dots$) depend on the reflection and transmission coefficients contained in the matrices $\mathcal{R}_{n\pm}$ and $\mathcal{T}_{n\pm}$ ($n = 1, 2$). Expression (3.6) is expected to be valid for sufficiently large separations, and not around the resonances where the role of the evanescent waves cannot be neglected in the interaction theory. The zeroth order approximation is clearly identical to (3.4). In principle, it would also be possible to formulate an expression analogous to (3.6) that includes evanescent waves.

In the right-hand panels of figure 4 the log-averaged energy transmitted by two cracks is shown as a function of the lower limit of their separation. A uniform distribution over half a wavelength is used for the separation of the two cracks. The three wave periods $\tau = 8$ s, 12 s and 16 s are shown by the different panels.

Three different curves are compared in each panel. The crosses are results from an ensemble average, calculated using the relations (3.2), for an approximation that includes the propagating and the damped-propagating waves. It is evident that the damped-propagating waves have an influence on the transmitted energy for separations below approximately $s_0 = 150$ m for all three wave periods, although this is negligible in the 16 s period case until approximately $s_0 = 50$ m. The grey curves are the corresponding converged approximations that include a sufficient number of the evanescent waves. They differ from the previous approximation for separations below approximately 100 m for 8 s and 12 s wave periods, but are indistinguishable for 16 s period.

The black-broken curves are the second-order approximations (in orders of K) given by the analytic expression (3.6). These curves follow their corresponding ensemble averages (crosses) for an interval of separations in which the damped-propagating waves are significant. However, as would be expected, the second-order approximations lose accuracy when the cracks become closer. Although it is possible to extend this interval by increasing the order of the approximation, it has been found that the convergence is poor due to growth in certain terms.

In order for the expression (3.6) to be used for more than two features, expressions for the average values of the remaining reflection and transmission coefficients contained in the matrices $\mathcal{R}_{1,2\pm}$ and $\mathcal{T}_{1,2\pm}$ must also be produced. The subsequent relations could then be applied repeatedly, with no averaging required, to obtain an attenuation coefficient. This process is, however, more cumbersome than that for the WSA due to the complicated expressions for the coefficients c_n ($n = 1, 2, \dots$). Unfortunately, no

useful simplifications, such as a weak-scattering approximation, appear to be applicable here.

In reality, most pressure ridges are separated (peak to peak) by 80 m to 300 m (Davis & Wadhams, 1995), and the separation of cracks is typically on the order of kilometres (Sear & Wadhams, 1992). The latter statement is deduced from information about the separation of leads, which are regarded as originating from cracks, and are more easily detected. Therefore, for a practical application, it is appropriate to use a WSA to calculate the wave interactions between cracks and ridges, as well as floes. If an attenuation coefficient is required for a region in which it is known that the separation of features is small, then the full approximation (including damped-propagating and evanescent waves) must be applied.

Of practical importance for the present application is the accommodation of damping over intervals of ice-covered fluid, in conjunction with a WSA. To do this, the expression for the attenuation coefficient, given in equation (3.5), must be modified to account for the additional damping process. Therefore, consider once more the logarithmic average of the transmitted energy produced by two adjacent features, using the WSA, but now allowing for a small imaginary component in the primary wavenumber. From the second element of (3.2) it follows that

$$\langle \langle \log |T_{1,2-}|^2 \rangle \rangle = \langle \langle \log |T_1 - T_{2-} e^{i(\kappa_0 + i\epsilon)s}|^2 \rangle \rangle - \langle \langle \log |1 - R_{1+} R_{2-} e^{i(\kappa_0 + i\epsilon)s}|^2 \rangle \rangle.$$

The first term on the right-hand side of this identity can be evaluated to be $\langle \log |T_1 - T_{2-} e^{-\epsilon \hat{s}}|^2 \rangle$, which differs from its non-damped counterpart only through the presence of the exponential term. The second integral vanishes when the primary wavenumber is real. However, when a small imaginary component is included its contribution is non-zero and its value can be sought by expanding the logarithm as a series, which shows, up to terms of order $\langle e^{-4\epsilon \hat{s}} \rangle$, that

$$\langle \langle \log |1 - R_{1+} R_{2-} e^{i(\kappa_0 + i\epsilon)s}|^2 \rangle \rangle = \left\langle -\frac{4}{\lambda} \text{Im} \left\{ \frac{R_{1+} R_{2-}}{\kappa_0 + i\epsilon} e^{2i\kappa_0 \hat{s}} \right\} \sinh \left(\frac{\epsilon \lambda}{2} \right) e^{-2\epsilon \hat{s}} \right\rangle.$$

Its contribution is therefore exponentially small, and it is reasonable to discard it. Hence, the log-averaged transmitted energy for two features, when damping is included, is

$$\langle \langle \log |T_{1,2-}|^2 \rangle \rangle \approx \langle \log |T_1|^2 \rangle + \langle \log |T_{2-}|^2 \rangle - 2\epsilon \hat{s}. \quad (3.7)$$

Repeated application of this expression then defines the attenuation coefficient to be

$$\mu = -\langle \log |T_{0-}|^2 \rangle + 2\epsilon \hat{s}. \quad (3.8)$$

This merely states that the contributions to the attenuation coefficient of the scattering produced by features and the damping that occurs between the features are distinct. Of course, an additional imaginary damping component in the fluid-ice coupling (2.3) may affect the values of the transmission coefficients for the individual features. This will be studied in § 4.

The right-hand panel of figure 2 shows the attenuation coefficient as a function of wave period for a 3 m-thick QCIC containing cracks. The distribution of the crack separation is uniform in the interval 100 m to 100 m + $\lambda/2$. Damping is also produced by an imaginary component in the primary wavenumber, which is of magnitude $\epsilon = 10^{-4}$. The distance between cracks is therefore a determinant of the attenuation rate.

Results are shown for the arithmetic and geometric means, using ensemble averages. The semi-analytic expression (3.8) is also overlaid. It is clear that the damping effect

is dominant for the larger wave periods, and consequently the arithmetic and geometric averages coincide. For smaller wave periods, the scattering produced by the cracks is the most important process. The minimum between these two regimes, at approximately an 11 s wave period, corresponds to perfect transmission by the individual cracks. These types of sensitivity to the geometrical configuration will be reduced by averaging the properties of the individual features, and is investigated in § 4.

4. Modelling individual features

It is possible to calculate the scattering properties of the individual features using a number of methods. The interaction theory outlined in the previous section only requires that the method produces the value of the transmission coefficient for situations in which the WSA is applicable, and the relevant scattering matrices otherwise.

For the purpose of the present investigation, an approximation method will be applied, which is based on the combination of a Hamiltonian variational principle and a projection of the vertical fluid motion onto a $(P + 1)$ -dimensional trial space ($P \geq 0$), spanned by a finite set of the relevant vertical modes, $\{\eta_0, \dots, \eta_P\}$ or $\{\xi_0, \dots, \xi_P\}$. It has been used previously for a number of hydroelastic geometries (e.g. Bennetts et al., 2007; Vaughan et al., 2009). The dimension of the trial space required to produce accurate scattering properties has been investigated in a number of these works.

The two-dimensional features that are considered in this work are susceptible to resonant responses, in which their reflection and transmission vary rapidly over small parameter intervals. Such resonances are a product of the highly idealised geometries assumed for the individual features, and are not thought to be indicative of the physical problem being modelled. A better representation of the scattering properties of an individual feature can be obtained by calculating an ensemble average, in which properties are selected from a prescribed distribution. However, this greatly increases the numerical expense and adds noise. It is therefore judicious to avoid this procedure where possible.

One compensation for situations in which averaging is required is that a relatively large dimension of the trial space is often necessary to resolve the resonances. As averaging is used here to smooth these resonances away, it is conjectured that accurate results will be possible with smaller dimensions. Note that the dimension of the trial space, $P + 1$, is independent of the number of waves used in the interaction theory between features, $N + 1$, although it is required that $P \geq N$.

The introduction of an artificial damping term on the energy transmitted by the features will also be considered. To do this, the fluid-ice coupling (2.3a) is modified, as in Vaughan et al. (2009), through the addition of an imaginary component that is proportional to the velocity of the interface, so that

$$(1 - \sigma d - i\gamma)w + Fw'''' = \phi \quad (z = -d).$$

The quantity γ is a function of angular frequency, and is defined as $\gamma = \omega\Gamma/(g\rho_w)$. All non-negative values of Γ are admissible, but the value $\Gamma = 1.5 \times 10^3 \text{ Pa s m}^{-1}$ has been used for particularly slushy ice (see Vaughan et al., 2009), and therefore provides an upper bound for the present study. By comparing to the best data sets currently available (e.g. Wadhams et al., 1988), it has been found that a value of $\Gamma = O(10)$ is more appropriate. (The units of Γ have been omitted here and subsequently for clarity.)

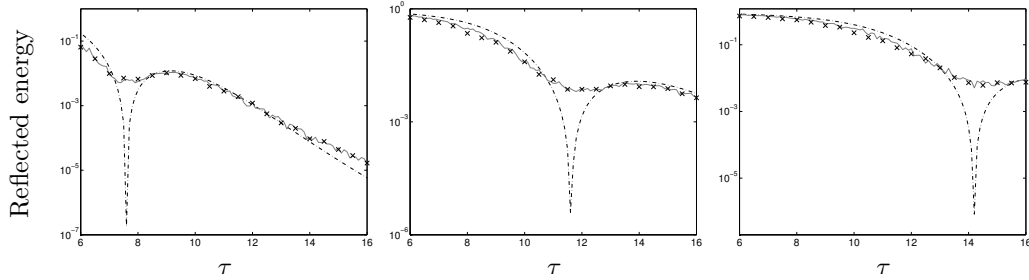


Figure 5. The energy reflected by an individual crack, as a function of wave period. The ice thickness is 1 m (left panel), 3 m (middle) and 5 m (right). Unaveraged results are denoted by the black-broken curves and results from an ensemble average, in which the ice thickness obeys a Gaussian distribution, are denoted by the grey curves. Results for a similar ensemble that includes a damping term ($\Gamma = 10^3$) are denoted by the crosses.

(a) Cracks

Geometrically, cracks only depend on the surrounding ice thickness, and we may write $T_0 = T_0(D_L, D_R)$, etc., where D_L and D_R are the ice thicknesses to the left and right of the crack, respectively. The logarithmic average of the transmitted energy is therefore

$$\langle \log |T_{0-}|^2 \rangle = \int_0^\infty \int_0^\infty p_D(D_L) p_D(D_R) \log |T_{0-}|^2 dD_L dD_R,$$

where p_D is the probability distribution of the thickness on one side of the crack, which is assumed to be identical on either side of the crack.

The scattering properties of a single crack contain a unique resonant point at which perfect transmission occurs. Instances of this behaviour are shown by the black-broken curves of figure 5, which denote unaveraged data. The reflected energy is given rather than transmitted energy, as it more clearly displays the resonant behaviour. In any case, these values could be used in place of the transmitted energy, due to the identity $|R_{0\pm}|^2 + |T_{0-}T_{0+}| = 1$, and symmetry. It is evident that the period at which perfect transmission occurs increases as the surrounding ice becomes thicker, which is caused by the flexural response of the ice dominating over its mass loading for a greater range of periods (the former being proportional to D^3 and the latter to D , see Vaughan et al., 2007). The qualitative properties of the results are otherwise as expected, with monotonically decreasing reflection, i.e. increasing transmission, as wave period becomes larger.

Results calculated from an ensemble average of 100 simulations, in which the ice thickness obeys a Gaussian distribution, are also presented in figure 5 (grey curves). The mean values match the corresponding unaveraged data, and the standard deviation is set as one-third of this mean thickness. Although the averaging process significantly smooths the resonances, even with the large standard deviation used here, a shallow concavity remains in their place. For the results presented in figure 5, 8 to 16 evanescent waves were included in the approximation to produce satisfactory convergence for the averaged data, compared to 64 to 128 for the unaveraged data. It is noted that a WSA can also be applied for a crack and would give good accuracy (see Vaughan et al., 2007).

As an individual crack has no length, the effects of including viscous damping are expected to be small. This is confirmed by the data represented by crosses in figure 5, which give corresponding ensemble averages in which a large viscous term, $\Gamma = 10^3$, is included. As noted earlier, the appearance of an imaginary term in the fluid-ice coupling displaces the roots of the ice-covered dispersion relation off of the real/imaginary axes. It is therefore necessary to use an iterative method to obtain both the real and imaginary components of the perturbed roots, which increases the numerical expense. Whilst this extra computational load goes virtually unnoticed for an individual simulation, the run-times for ensemble averages, especially over large parameter ranges, are greatly increased. The ability to disregard viscous damping is hence a significant benefit.

(b) *Floes*

Floes are defined by their thickness and length, and it is therefore possible to average over both of these dimensions. It is convenient to consider the scattering response of an individual floe as a combination of the responses of its two ends. That is, given a floe thickness, reflection and transmission matrices are calculated for the ends of the floe in isolation, which are, of course, symmetric, and independent of length. The scattering matrices for a floe of any prescribed length may then be obtained through a single application of relations (3.1). Moreover, the number of waves used in the interaction theory between the two ends of the floe does not have to be equal to the dimension used to calculate the scattering matrices at the ends. As seen during the analysis of multiple features in a QCIC, the number of waves required in the interaction theory depends on the ice thickness, the wave period and the separation of the scatterers (here the ends of the floe).

The behaviour of a floe with respect to its length is very similar to that of the separation of two features in a QCIC. For each thickness and period, there exists a length, usually below 200 m, beyond which the wave interactions within the floe depend only on the propagating waves, i.e. a WSA is valid. For an interval of lengths prior to this the interaction theory must be supplemented with the damped-propagating waves. However, it is possible for wave interactions consisting only of the propagating and damped-propagating waves to produce spurious resonances when the floe length is small, and a number of evanescent waves must be included to capture accurate results.

Two examples of this behaviour are given in figure 6. The results display different approximations to the energy transmitted by an individual floe, as a function of its length, l . The left-hand panel shows results for relatively strong scattering, with ice thickness 4 m and wave period 8 s. The converged approximation (black curve) uses 8 evanescent waves in addition to the damped-propagating and propagating waves. It is evident in this case that a WSA (light-grey curve) is valid for lengths greater than approximately $l = 200$ m. An approximation that includes only the damped-propagating and propagating waves, marginally extends the validity of the WSA, to approximately $l = 150$ m.

The right-hand panel shows results for a problem that produces weaker scattering, with ice thickness 1 m and wave period 12 s. A converged solution now only requires the damped-propagating waves in addition to the propagating waves. No spurious resonances are encountered. The WSA is valid from approximately $l = 100$ m onwards.

Similarly to § 3, wave interactions within floes are essentially governed by the phase of the propagating wave. Following the reasoning outlined for multiple features, an average is taken of the phases, corresponding to half an (ice-coupled) wavelength. A set of results for the log-averaged transmitted energy as a function of the lower bound of floe

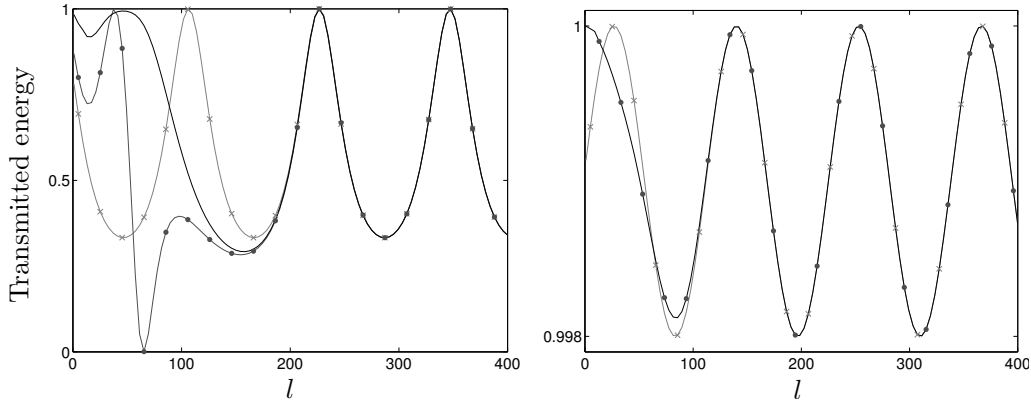


Figure 6. Comparisons of the approximate transmitted energy for an individual floe, as a function of its length. The floe thickness and wave period are, respectively, 4 m and 8 s (left-hand panel), and 1 m and 12 s (right-hand panel). The WSAs are shown by the light-grey curves with crosses, the approximations that also includes the damped-propagating waves are the dotted dark-grey curves, and the black curves are converged approximations (overlaps dark grey in right panel).

length, l_0 , is shown in figure 7 (solid-grey curves). The data are calculated from ensemble averages of 100 simulations, and floe thicknesses 1 m, 2 m and 4 m and wave periods 8 s and 12 s are considered. The dimension of the approximation for the individual ice edges and the number of waves used for the interaction theory are sufficient to produce convergence. For the ice edges the dimension ranges between $P = 4$ to 64, and is typically larger for thicker ice and/or a smaller period, as expected. The number of evanescent waves used in the interaction theory, in addition to the damped-propagating and propagating waves, is up to 8, and is also typically larger for thicker ice and/or a smaller period, as well as depending on floe length.

In each case the transmitted energies produced by the ensemble averages settle to a constant value after a certain floe length that corresponds to the point at which the WSA is valid. This constant value can be calculated by exactly the same manipulations that led to expression (3.4), and produces

$$\langle \log |T_{0-}|^2 \rangle = \log |t_-|^2 + \log |t_+|^2, \quad (4.1)$$

where t_{\pm} are the transmission coefficients for a single ice edge, with a wave incident from the open water (-) and from the ice-covered fluid (+), respectively. Note that the expression on the right-hand side of (4.1) may be replaced by $2 \log(1 - |r|^2)$, where r is the reflection coefficient for either of the incident waves, so that only one of them need be considered.

Higher-order approximations analogous to (3.6) that account for the damped-propagating waves can also be formulated, and second-order approximations are overlaid on the panels of figure 7 (black-broken curves). Recall that these approximations tend to the zeroth-order approximation (4.1) when the floe length is sufficiently large.

Consistent with the case of multiple features in a QCIC, the point at which the WSA is valid depends on both the ice thickness and the wave period. In particular, the thicker the floe, the longer it must be for the WSA to be accurate. In the examples shown here, it is usually valid by a length of 200 m, but can be far shorter for thinner ice.

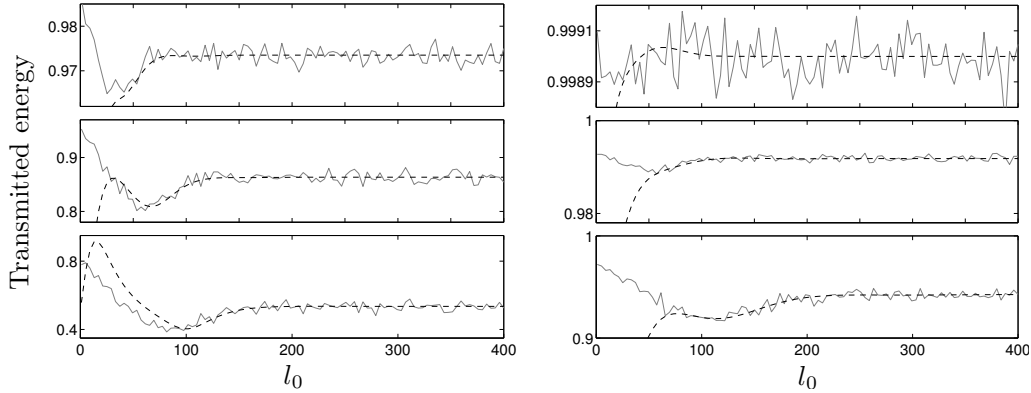


Figure 7. The energy transmitted by an individual floe, as a function of the lower limit of its length. The wave period is 8 s (left-hand panels), and 12 s (right). The ice thickness is 1 m (top panels), 2 m (middle) and 4 m (bottom). The solid-grey curves are calculated using ensemble averages, in which the floe length distribution is uniform over half a wavelength. The black-broken curves are second-order approximations in terms of the decaying component of the damped-propagating waves.

As expected, the second-order approximations extend the intervals over which the semi-analytic expressions are valid, compared to (4.1). This is most evident for the cases in which scattering is significant. The corresponding curves in figure 7 are very close for all l_0 greater than at least 100 m. However, it is also evident that the second-order approximations can be highly inaccurate for small floe lengths.

Thus far, for each ensemble the ice thickness has been held constant and no resonant behaviour has been detected. This is a consequence of the non-zero draught of the floe. For a given floe that floats artificially on the surface of the fluid, often referred to as a shallow-draught approximation, there exists a unique resonant period at which perfect transmission of a normally incident wave occurs. This is analogous to the perfect transmission produced by a crack. However, it is known that when an Archimedean draught is included this resonance is eliminated (Williams & Porter, 2009), and is actually displaced into the oblique incidence regime.

It may therefore be inferred that no averaging over the thickness of the floe is required. This is confirmed by results shown in the left-hand panels of figure 8, which compares unaveraged values for the energy reflected by an ice edge with corresponding ensemble averages. Two thicknesses are considered and the standard deviation used for the ensembles is one-third of the relevant mean thickness. In both cases, the ensembles are almost identical to the corresponding unaveraged data.

It is therefore possible to calculate the attenuation coefficient, μ , for MIZ conditions, from the canonical problem of wave scattering by a single ice edge, assuming floes of sufficient length that the WSA is valid. This assumption mirrors the long-floe approximation adopted by Wadhams (1986) and Kohout & Meylan (2008). The value of the attenuation coefficient is then simply

$$\mu = -2 \log(1 - |r|^2).$$

Results for the energy reflected by an ice edge when damping is included are also shown in the left-hand panel of figure 8 (crosses), with $\Gamma = 10^2$ here. As with the case of cracks, the inclusion of damping has a very small effect on the reflection. However,

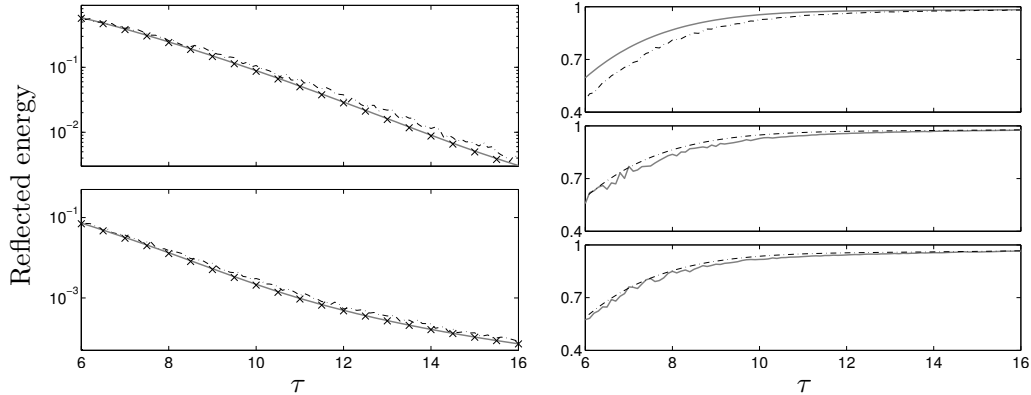


Figure 8. The left-hand panels show the energy reflected by a single ice edge, as a function of wave period. The ice thickness is 1 m (top panel) and 4 m (bottom). The grey curves are unaveraged results. The black-broken curves are results calculated using an ensemble average, in which the ice thickness obeys a Gaussian distribution. Unaveraged results, in which damping is included ($\Gamma = 10^2$) are denoted by the crosses. The right-hand panels show the energy transmitted by an individual floe, as a function of wave period, and including damping. The lower bound of the floe length is 50 m (top panel), 100 m (middle) and 200 m (bottom). The grey curves are results calculated from ensemble averages, in which the floe-length distribution is uniform over half a wavelength, and the black-broken curves are the corresponding semi-analytic approximations, which assume the WSA.

the imaginary component will induce decay over the length of the floe. This may be accounted for in the interaction theory, so that the reflection and transmission matrices are calculated from the isolated ice edge without damping ($\Gamma = 0$), but the loss of wave energy over the length of the floe is achieved by using the roots of the dispersion relation (with the appropriate value of Γ) in the matrix Λ . When the WSA is applied the semi-analytic expression (4.1) may be simply modified in the same manner that produced (3.7).

The panels on the right-hand side of figure 8 show examples of how the WSA of the transmitted energy (black-broken curves) compare to ensemble averages (grey curves), when damping is included. Three lower limits of floe length are considered, $l_0 = 50$ m (top panel), 100 m (middle) and 200 m (bottom), and the ice thickness is set as 2 m in all cases. As expected, the approximation is least accurate for the shortest floe length and for the smallest periods, due to the influence of the damped-propagating waves in the interaction theory. The approximation is otherwise very close to the data produced by the ensemble averages. Slight deviations are apparent around $\tau = 10$ s for the $l_0 = 100$ m and 200 m cases, which correspond to the maximum in the imaginary component of the primary propagating wave, undermining the assumption that the scattering matrices for the ice edge are unaffected by the damping term.

(c) Pressure Ridges

Pressure ridges are complicated structures, displaying a large amount of variation in their shape, as well as their widths and heights. However, by analysing the available data for the properties of pressure ridges, Timco & Burden (1997) identify two typical cross-sectional ridge profiles. Approximate versions of these will be utilised in this section.

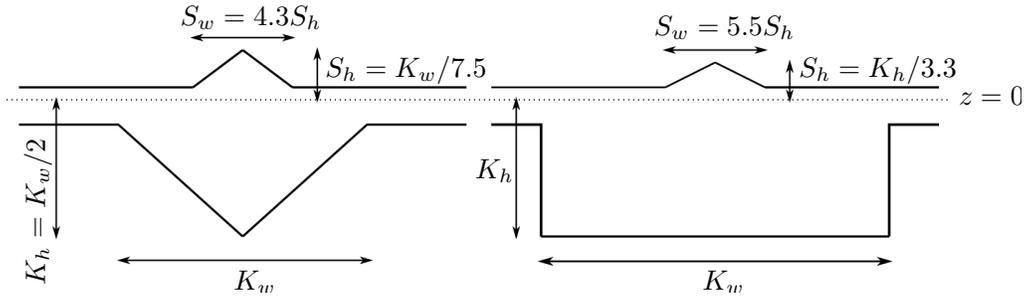


Figure 9. Profiles of a typical first-year ridge (FYR, left) and multi-year ridge (MYR, right).

The two classes of ridge are referred to as first-year ridges (FYRs) and multi-year ridges (MYRs). Both display variations in their upper and lower surfaces, known as sails and keels, respectively. The profiles of FYRs and MYRs are distinguished mainly through the shape of their keels, with the former being roughly triangular, and the latter roughly rectangular. Both have triangular sails that are of smaller area than their respective keels.

The profiles of the FYRs and MYRs that will be used in this investigation are shown in figure 9. Notice that the dimensions of the FYR is determined by specifying any one of its sail height or width, or keel height or width. The data used by Timco & Burden (1997) contain FYR keel widths ranging from approximately 10 m to 150 m, with most lying in the interval 10 m to 30 m. In comparison, the MYR requires the specification of both a height and a width. Timco & Burden (1997) are only able to provide information on keel heights, these being approximately 5 m to 40 m, with most around 10 m, although cross-sectional areas of the keels are also provided, these being at greatest 1500 m^2 , but usually below 1000 m^2 .

It is evident that the typical MYR shown on the right-hand side of figure 9 closely resembles a rectangular ridge. Motivated by this, a mapping of a MYR to a rectangular ridge was sought, and it was found that a rectangular ridge with the same keel but with a rectangular sail of height one-tenth that of the keel and the same width, produces nearly identical scattering properties to a MYR for the range of dimensions and frequencies under consideration. The rectangular ridge is computationally efficient as it possesses only two interfaces, compared to the MYR that must be discretised to some given tolerance. The mapped rectangular ridge is therefore used in the computations presented in this work. The corresponding results produced by the exact MYR profiles are given in the right-hand panels of figure 10 for comparison (asterisks).

Examples of the energy transmitted by FYRs and MYRs, as functions of wave period, are shown in figure 10. The left-hand panels show results produced by FYRs, with the top panel those for a smaller ridge, of width $K_w = 20 \text{ m}$, in ice of otherwise constant 1 m thickness. The bottom panel is for a larger ridge, of width $K_w = 50 \text{ m}$, in ice of otherwise constant 3 m thickness. The right-hand panels use MYRs, with, again, the top panel being for a smaller ridge, $K_w = 20 \text{ m}$, $K_h = 10 \text{ m}$ and surrounding thickness 1 m, and the bottom panel for a larger ridge, $K_w = 40 \text{ m}$, $K_h = 30 \text{ m}$ and surrounding thickness 3 m.

For each panel, unaveraged results are given (black curves), as well as results calculated from an ensemble average (grey). In the ensemble the widths obey a

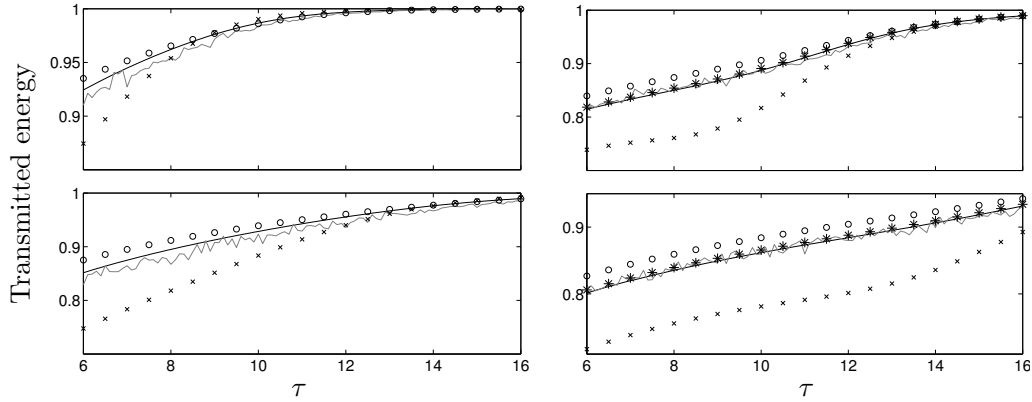


Figure 10. The energy transmitted by individual ridges, as a function of wave period. The left-hand panels are results for FYRs, of width 20 m (top panel), and 50 m (bottom). The right-hand panels are results for MYRs, of width 20 m and height 10 m (top panel), and width 40 m and height 20 m (bottom). Unaveraged results are shown by the black curves and results calculated from ensemble averages, in which the ridge dimensions obey a Gaussian distribution, are shown by the grey curves. The corresponding unaveraged results for unmapped MYRs are denoted by asterisks. Unaveraged results are also shown for Young's moduli $Y = 1 \text{ GPa}$ (crosses) and $Y = 10 \text{ GPa}$ (circles).

Gaussian distribution with a mean value corresponding to the unaveraged case and a standard deviation one-third that of the mean width. No resonant behaviour is visible in the unaveraged results shown in the examples presented in figure 10, and none has been found in tests conducted by the authors for relevant parameter values. This is unsurprising as length resonance is precluded by the stiffness of the ridge. The results calculated from the ensembles are therefore, as expected, very close to their unaveraged counterparts. It is concluded that no averaging is necessary for individual ridges. The dimensions used for the approximations in these examples span $P = 4$ to 32, depending on the wave period and the size of the ridge. These are typical values for realistic parameter ranges.

The crosses and circles on figure 10 denote corresponding unaveraged results for a Young's modulus of 1 GPa, and 10 GPa, respectively. Although this is not intended as a definitive investigation of the sensitivity of attenuation to the Young's modulus, variation in this parameter is anticipated to be particularly relevant in the case of FYRs and MYRs. The examples here indicate that a reduction in the Young's modulus has the most pronounced effect, particularly for small wave periods and MYRs.

The final investigation concerns the effects of damping on the energy transmitted by FYRs and MYRs. The left panels of figure 11 compare the energy transmitted by ridges without (black curves) and with (crosses) damping, the latter again using a value of $\Gamma = 10^2$. As the effects of damping are proportional to the scattering produced by a feature, results for the smaller ridges used in figure 10 are presented.

Although the differences between the corresponding damped and undamped results are very close to one another, there is a clear difference between them, particularly for the FYR (top panel). It is also evident that results differ most for large periods, that is, periods at which scattering is small. However, note that the differences shown here are for a relatively large damping parameter, Γ .

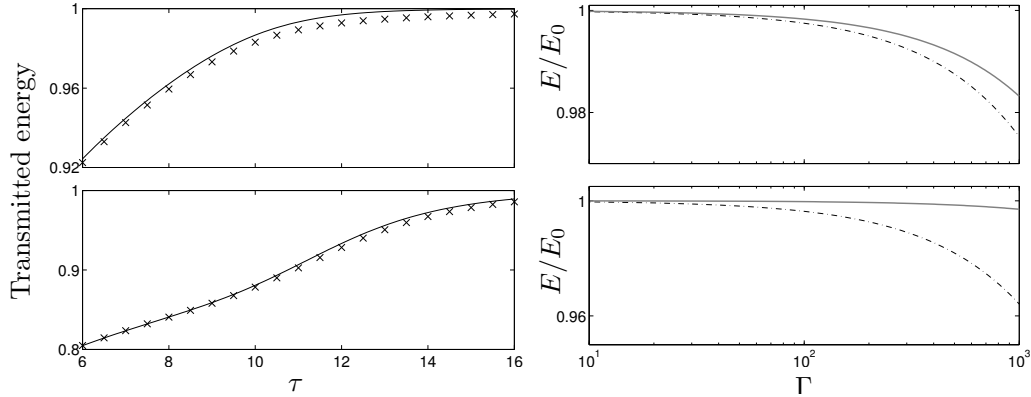


Figure 11. The left-hand panels show the energy transmitted by individual ridges, as a function of wave period. The results in the top panel are for a FYR of width 20 m, and on the bottom panel are for a MYR of width 20 m and height 10 m. The solid curves show the undamped case and the crosses are the case in which $\Gamma = 10^2$. The right-hand panels show the corresponding ratios of the transmitted energy including damping to the transmitted energy without damping, as a function of the damping parameter. Converged approximations are shown by the black-broken curves and approximations that neglect scattering are shown by the grey curves.

In order to ascertain the regime in which the transmitted energy produced by the ridges must account for damping, the right-hand panels of figure 11 show the corresponding ratios of the damped transmitted energy, $E = E(\Gamma)$, to the undamped transmitted energy, $E_0 \equiv E(0)$, as a function of the damping parameter. The largest period in the range, $\tau = 16$ s, is used as it produces the most pronounced difference between the damped and undamped cases.

For both ridges, the ratio E/E_0 is linear with respect to Γ (the abscissa is scaled logarithmically). Even for the largest value of Γ the difference between the transmission produced by the damped and undamped models is only, at most, four percent. However, it has been found for damping parameters of the order 10^3 that significant differences can be produced for smaller periods. At $\Gamma = 10$ the damped and undamped transmitted energies agree to four significant figures. It is therefore only necessary to include damping for individual ridges, when the damping parameter becomes large, $\Gamma \approx O(10^2)$.

Approximations are also included in the right-hand panels of figure 11, which give an estimate of the damping that is expected if scattering is ignored (grey curves). This is calculated from the imaginary component of the primary wavenumber. For the MYR, which is mapped to a rectangular ridge, this is straightforward, as the ridge has constant thickness. However, the thickness of the FYR varies across its length, and the mean of the wavenumber over its profile is therefore used. This results in a very good agreement, whereas the approximation for the MYR is far worse, indicating that scattering is still significant for the MYR at a 16 s wave period, which may be attributed to the large jump in thickness that occurs at its edges.

5. Conclusions and implications for integration into OGCMs

As signalled in § 1, a strand of the current work is to assimilate wave-ice interactions into an operational ice/ocean model and, potentially, an OGCM. This project is underway, with derived scattering kernels being synthesized into a set of look-up tables that allow wave attenuation to be determined straightforwardly for sea ice data products furnished by satellite or other sources. Because each look-up table is accessed many times, efficiency relies on minimising its dimension.

In summary, the outcomes of the reported study are

1. A WSA between MIZ floes provides extremely high accuracy for all relevant parameter values; floe separation just alters phase, creating periodicity in the transmitted energy that can be overcome by giving the inter-floe phase a uniform distribution corresponding to similarly distributed separations. Logarithmic averaging produces a semi-analytic expression that allows the attenuation coefficient to be found from knowledge of the scattering from an individual floe alone.
2. Wave energy is conserved between floes, so averaging results in a non-dimensional attenuation coefficient that is insensitive to concentration and maps directly onto the dimensional coefficient used in OGCMs.
3. Primarily because of the damped-propagating waves, the WSA is only valid in the QCIC when features are more than a specific distance apart that is greater for cracks than pressure ridges and typically < 200 m but depends on period and thickness.
4. Inelastic damping can be accommodated between QCIC features. Because scattering and damping are distinct, the modification is simple and the OGCM look-up table is not required to describe how attenuation varies with damping.
5. If the WSA holds, the look-up table only needs to carry information on the transmission properties of individual features.
6. The consequences of unwanted resonant behaviour that leads to perfect transmission through cracks can be reduced by statistically distributing ice thicknesses and averaging, noting also that cracks are unresponsive to the inclusion of inelastic damping.
7. Floe behaviour with respect to length is similar to that of QCIC feature separation. A WSA is valid for floes of sufficient length, depending on the wave period and thickness and, beyond this limit, the average transmission of an individual floe is insensitive to its length and can be found from the reflection at an edge with no thickness averaging being required because draught is included. This considerably reduces the amount of information that must be stored on floes in an OGCM.
8. Pressure ridges were assigned two typical profiles, referred to as FYRs and MYRs. No averaging of their properties is required and damping needs to be considered only rarely.

A sensitivity analysis is now essential to minimise the dimensions in any OGCM look-up tables. Moreover, alternative damping models that assimilate more general

inelasticity need to be explored. To finish, we observe again that the advent of an operational model that includes ocean wave interactions highlights the lack of up-to-date detailed field data to support these theoretical advances.

Acknowledgment

This study is part of Waves-in-Ice Forecasting for Arctic Operators, funded by the Research Council of Norway and Total E&P Norge. The authors are grateful for this support and that of the University of Otago

References

- Bennetts, L. G., Biggs, N. R. T., Porter, D., 2007. A multi-mode approximation to wave scattering by ice sheets of varying thickness. *J. Fluid Mech.* 579, 413–443.
- Bennetts, L. G., Peter, M. A., Squire, V. A., Meylan, M. H., 2010. A three-dimensional model of wave attenuation in the marginal ice zone. *J. Geophys. Res.* 115 (C12043).
- Berry, M. V., Klein, S., 1997. Transparent mirrors: rays, waves and localization. *Eur. J. Phys.* 18, 222–228.
- Davis, N. R., Wadhams, P., 1995. A statistical analysis of Arctic pressure ridge morphology. *J. Geophys. Res.* 100 (C6), 10915–10925.
- Dumont, D., Kohout, A. L., Bertino, L., 2011. A wave-based model for the marginal ice zone including a floe breaking parameterization. *J. Geophys. Res.* 116 (C04001).
- Kohout, A. L., Meylan, M. H., 2008. An elastic plate model for wave attenuation and ice floe breaking in the marginal ice zone. *J. Geophys. Res.* 113 (C09016).
- Krogstad, H. E., 2005. Measuring and analysing the directional spectrum of ocean waves. COST Action 714, EUR21367, Luxembourg, Ch. The directional wave spectrum, pp. 15–54.
- Kwok, R., Rothrock, D. A., 2009. Decline in Arctic sea ice thickness from submarine and ICESat records: 1958–2008. *Geophys. Res. Lett.* 36 (15).
- Sear, C. B., Wadhams, P., 1992. Statistical properties of Arctic sea ice morphology derived from sidescan sonar images. *Prog. Oceanogr.* 29 (2), 133–160.
- Serreze, M. C., Holland, M. M., Stroeve, J., 2007. Perspectives on the Arctic’s shrinking sea-ice cover. *Science* 315 (5818), 1533–1536.
- Squire, V. A., 2007. Of ocean waves and sea-ice revisited. *Cold Reg. Sci. Technol.* 49, 110–133.
- Squire, V. A., Dugan, J. P., Wadhams, P., Rottier, P. J., Liu, A. K., 1995. Of ocean waves and sea ice. *Annu. Rev. Fluid Mech.* 27, 115–168.
- Squire, V. A., Vaughan, G. L., Bennetts, L. G., 2009. Ocean surface wave evolution in the Arctic Basin. *Geophys. Res. Lett.* 36 (L22502).

- Timco, G. W., Burden, R. P., 1997. An analysis of the shapes of sea ice ridges. *Cold Reg. Sci. Technol.* 25, 65–77.
- Timco, G. W., Weeks, W. F., 2010. A review of the engineering properties of sea ice. *Cold Reg. Sci. Technol.* 60, 107–129.
- Toyota, T., Haas, C., Tamura, T., 2011. Size distribution and shape properties of relatively small sea-ice floes in the Antarctic marginal ice zone in late winter. *Deep Sea Res. Pt. II* 58 (9–10), 1182–1193.
- Vaughan, G. L., Bennetts, L. G., Squire, V. A., 2009. The decay of flexural-gravity waves in long sea-ice transects. *Proc. R. Soc. Lond. A* 465, 2785–2812.
- Vaughan, G. L., Williams, T. D., Squire, V. A., 2007. Perfect transmission and asymptotic solutions for reflection of ice-coupled waves by inhomogeneities. *Wave Motion* 44, 371–384.
- Wadhams, P., 1973. The effect of a sea ice cover on ocean surface waves. Ph.D. thesis, Scott Polar Research Institute, University of Cambridge.
- Wadhams, P., 1986. The seasonal ice zone. In: Untersteiner, N. (Ed.), *The Geophysics of Sea Ice*. Plenum, New York, pp. 825–991.
- Wadhams, P., Davis, N. R., 2000. Further evidence of ice thinning in the Arctic Ocean. *Geophys. Res. Lett.* 27 (24), 3973–3976.
- Wadhams, P., Squire, V. A., Ewing, J. A., Pascal, R. W., 1986. The effect of the marginal ice zone on the directional wave spectrum of the ocean. *J. Phys. Oceanogr.* 16 (2), 358–375.
- Wadhams, P., Squire, V. A., Goodman, D. J., Cowan, A. M., Moore, S. C., 1988. The attenuation rates of ocean waves in the marginal ice zone. *J. Geophys. Res.* 93 (C6), 6799–6818.
- Wang, R., Shen, H., 2010. Gravity waves propagating into an ice-covered ocean: A viscoelastic model. *J. Geophys. Res.* 115 (C06024).
- Williams, T. D., Porter, R., 2009. The effect of submergence on the scattering by the interface between two floating plates. *J. Fluids. Struct.* 25 (5), 777–793.
- Williams, T. D., Squire, V. A., 2010. On the estimation of sea-ice thickness using wave observations. *Dynam. Atmos. Oceans* 49 (2–3), 215–233.